Radiogenic power and geoneutrino luminosity of the Earth and other terrestrial bodies through time

W. F. McDonough[1,2], O. Šrámek[3], and S. A. Wipperfurth[1]

[1]Department of Geology, University of Maryland, College Park, MD 20742, USA
[2]Department of Earth Sciences and Research Center for Neutrino Science, Tohoku University, Sendai 980-8578, Japan
[3]Department of Geophysics, Faculty of Mathematics and Physics, Charles University, Prague, Czech Republic

Key Points:

- Radiogenic heat production and geoneutrino luminosity calculated over the age of the Earth
- Simple formulae proposed for evaluation at arbitrary planetary composition
- Differences in radioactive decay parameters highlighted between nuclear physics and geological communities

Corresponding author: W. F. McDonough, mcdonoug@umd.edu

Abstract

We report the Earth's rate of radiogenic heat production and (anti)neutrino luminosity from geologically relevant short-lived radionuclides (SLR) and long-lived radionuclides (LLR) using decay constants from the geological community, updated nuclear physics parameters, and calculations of the β spectra. We carefully account for all branches in ^{40}K decay using the updated β^- energy spectrum from physics and an updated branching ratio from geological studies. We track the time evolution of the radiogenic power and luminosity of the Earth over the last 4.57 billion years, assuming an absolute abundance for the refractory elements in the silicate Earth and key volatile/refractory element ratios (e.g., Fe/Al, K/U, and Rb/Sr) to set the abundance levels for the moderately volatile elements. The relevant decays for the present-day heat production in the Earth (19.9 ± 3.0 TW) are from ^{40}K, ^{87}Rb, ^{147}Sm, ^{232}Th, ^{235}U, and ^{238}U. Given element concentrations in kg-element/kg-rock and density ρ in kg/m^3, a simplified equation to calculate the heat production in a rock is:

$$h\,[\mu\mathrm{W\,m^{-3}}] = \rho\left(3.387\times10^{-3}\,[\mathrm{K}] + 0.01139\,[\mathrm{Rb}] + 0.04607\,[\mathrm{Sm}] + 26.18\,[\mathrm{Th}] + 98.29\,[\mathrm{U}]\right)$$

The radiogenic heating rate of earth-like material at Solar System formation was some 10^3 to 10^4 times greater than present-day values, largely due to decay of ^{26}Al in the silicate fraction, which was the dominant radiogenic heat source for the first ~ 10 My. Decay of ^{60}Fe contributed a non-negligible amount of heating during the first ~ 15 My after CAI (Calcium Aluminum Inclusion) formation, interestingly within the time frame of core–mantle segregation. Using factors and equations presented here, one can calculate the first-order thermal and (anti)neutrino luminosity history of various size bodies in the solar system and exoplanets.

Plain Language Summary

The decay of radioactive elements in planetary interior's produces heat that drives the dynamic processes of convection (core and mantle), melting and volcanism in rocky bodies in the solar system and beyond. Uncertainties in the decay constants for elements with 10^5 to 10^{11} half-lives range from 0.2% to $\sim$ 4% absolute and about 1% to 4% relative when comparing data sources in physics and geology. These differences, combined with uncertainties in Q (heat of reaction) values, lead to diverging results for heat production and for predictions of the amount of energy removed from the rocky body by emitted (anti)neutrinos.

1 Introduction

Radioactive decay inside the Earth produces heat, which in turn contributes power to driving the Earth's dynamic processes (i.e., mantle convection, volcanism, plate tectonics, and potentially the geodynamo). The physics community, using the latest numbers from nuclear physics databases, provide estimates of the radiogenic power and geoneutrino luminosity of the Earth (Dye, 2012; Ruedas, 2017; Usman et al., 2015; Enomoto, 2006a; Fiorentini et al., 2007). These studies include comprehensive reviews of the fundamental physics of these decay schemes, covering both the energy added to the Earth and that removed by the emitted geoneutrino. This note draws attention to differences in decay constants as reported in the geological and physics literature and recommends the former as being more accurate and precise. The absolute accuracy of geological studies is underpinned by the ^{238}U decay constant (Jaffey et al., 1971) and their relative accuracies are based on multiple cross-calibrations for different decay systems on the same rocks and mineral suites. Improvements in measurement precision comes from repeated chronological experiments.

There are a number of naturally occurring short-lived (relative to the Earth's age; half-lives $t_{1/2} < 10^8$ years) and long-lived ($t_{1/2} > 10^9$ years) radionuclides; those dis-

cussed here have half-lives between 10^5 and 10^{11} years. The long-lived decay constants are listed in Table 1 along with their decay modes and decay energies. The decay modes include alpha (α), beta-minus (β^-), and electron capture (EC). The beta-plus (β^+) decay mode is less common, but is seen in the ^{26}Al system, as well as a few minor branches in the Th and U decay chains and also likely in the ^{40}K branched decay. Geoneutrinos are naturally occurring electron antineutrinos ($\bar{\nu_e}$) produced during β^- decay and electron neutrinos (ν_e) produced during ε (i.e., β^+ and EC) decays. The generic versions of these decay schemes are:

$$\begin{aligned}
\text{Alpha} \quad (\alpha) \qquad & {}^{A}_{Z}X \rightarrow {}^{A-4}_{Z-2}X' + \alpha + Q, \\
\text{Beta Minus} \quad (\beta^-) \qquad & {}^{A}_{Z}X \rightarrow {}^{A}_{Z+1}X' + e^- + \bar{\nu}_e + Q, \\
\text{Electron Capture} \quad (\text{EC}) \qquad & {}^{A}_{Z}X + e^- \rightarrow {}^{A}_{Z-1}X' + \nu_e + Q, \\
\text{Beta Plus} \quad (\beta^+) \qquad & {}^{A}_{Z}X \rightarrow {}^{A}_{Z-1}X' + e^+ + \nu_e + Q, \\
\varepsilon \qquad & \text{refers to the combination of EC and } \beta^+
\end{aligned} \tag{1}$$

with parent element X, daughter element X', mass number A, atomic number Z, energy of reaction Q, electron e^-, positron e^+, and alpha particle α ($^4_2$He nucleus).

We report here radiogenic heat production and (anti)neutrino luminosity from geologically relevant short-lived radionuclides (SLR) and long-lived radionuclides (LLR). For the LLR we compare half-lives used in the geological and nuclear physics communities and recommend use of the former. We calculate the heat added to the Earth by these nuclear decays, as well as the energy carried away by (anti)neutrinos that leave the Earth. We calculate estimates of the embedded and removed energy of decay, particularly for the SLR, from β decay spectra calculated using Fermi theory and shape factor corrections. We conclude by presenting models for the Earth's radiogenic power and geoneutrino luminosity for the last 4568 million years, along with simple rules for extrapolating these results to other terrestrial bodies and exoplanets.

2 Contrasting methodologies

In compiling the data needed to calculate all of the observables, we found differences between the decay constants ($\lambda = \ln 2/t_{1/2}$) reported by the geological and nuclear physics communities. Values for extant systems are provided in a side-by side comparison in Table 2. The rightmost column reports the relative difference, in percent, between the decay constants from these communities and for some, the difference can be considerable (more than 30%). An updated physics number for the half-life of ^{190}Pt reported in Braun et al. (2017) agrees with the numbers obtained by Cook et al. (2004), who presented a detailed study of a suite of well behaved (closed system evolution), 4.5 billion year old, iron meteorites (i.e., group IIAB and IIIAB).

There is a 1.1% difference in the decay constant for ^{40}K between literature sources, which is a nuclide that provides $\sim$20 % of the planet's present-day radiogenic heat and $\sim$70 % of its geoneutrino luminosity (see Table 3). This difference is outside of the uncertainty limits on the half-life of ^{40}K, recently established by geochronologists (Renne et al., 2011).

Differences in decay constants reported by the geological and nuclear physics communities come from the methods used to establish the absolute and relative half-lives. Physics experiments typically determine a half-life value by measuring the activity $A = -dN/dt = \lambda N$ (N is the number of atoms) of a nuclide over time, whereas geochronology studies empirically compare multiple decay systems for a rock or suite of rocks that demonstrate close system behavior (show no evidence of loss of parent or daughter nuclide). The number of atoms N of parent nuclide evolves according to $N = N_0 e^{-\lambda t}$,

therefore $\ln N = \ln N_0 - \lambda t$. A plot of $\ln N$ (ordinate) vs. t (abscissa) gives a line of slope $-\lambda$ with y-intercept equal to $\ln N_0$.

Direct counting experiments generally involve the isolation of a pure mass of the parent nuclide of interest, knowing exactly the number of parent atoms at the start of the experiment, and then determining the ingrowth of daughter atoms produced at one or more times later (Begemann et al., 2001). Geochronological experiments compare multiple chronometric methods (e.g., U–Pb and K–Ar systems (Renne et al., 2011)) and develop a series of cross calibrations, where the shortcoming of this approach is the anchoring decay system that pins down the accuracy for other chronometers. It is recognized (Begemann et al., 2001; Villa et al., 2015; Ruedas, 2017) that the half-life of ^{238}U (Jaffey et al., 1971) is the most accurately known of the decay constants and thus acts as the anchor in these calculations. Table 2 highlights the differences in half-life values reported in a standard physics reference source NNDC (National Nuclear Data Center, `http://www.nndc.bnl.gov`) and geology. Relative differences at the $\sim 1\%$ scale and greater are seen for ^{40}K, ^{87}Rb, ^{176}Lu, ^{187}Re and ^{190}Pt decay systems.

Radioactive decay involves the transition to a lower level energy state of a nuclear shell and the accompanied release of energy, requiring the conservation of energy, linear and angular momenta, charge, and nucleon number. The kinetic energies of emitted alpha particles are discrete and on the order of 4 to 8 MeV, whereas different forms of beta decay show a continuous spectrum with characteristic mean and maximum energies for a given decay and the (anti)neutrino carrying away a complementary part of the energy. The energy of the beta decay process is partitioned between the electron, the antineutrino (or positron and neutrino), and the recoiling nucleus. Differences in heat production per decay reported in different studies are largely due to differences in decay energies (minimal differences), the energy carried off by (anti)neutrinos, and the branching fractions in the case of branched decays (large differences for the latter two). Furthermore, the time rate of heat production is sensitive to the value of the decay constant. This study differs from other recent efforts (Dye, 2012; Ruedas, 2017; Usman et al., 2015; Enomoto, 2006a; Fiorentini et al., 2007) in its input assumptions; we use decay constants and branching fractions from geochronological studies and we calculate the beta decay energy spectrum for most of the SLR and ^{40}K decays. For the remaining LLR decays, we adopt the energy spectra from Enomoto (2006b).

The ^{40}K decay scheme is a good example of where differences in inputs occur. Many naturally occurring decay schemes have a single decay mode, whereas ^{40}K is a branch decay scheme with β^- and ε decays (see Figure 1), with emission of an $\bar{\nu_e}$ and ν_e, respectively, removing energy from the Earth. The amount of radioactive heating in the Earth from this branch decay scheme depends on the branching ratio and the energy carried by the ν_e and $\bar{\nu_e}$. Using only geological data, Naumenko-Dèzes et al. (2018) examined the ^{40}K decay system and report a probability for the β^- branching between 89.25 % and 89.62 % and for the ε branching between 10.38 % and 10.75 %. They highlight that the errors on these values are non-Gaussian. The physics community reports the branching probabilities of β^- as 89.28(11) % and of ε as 10.72(11) % (Chen, 2017). Figure 1 reports the updated ^{40}K decay scheme—the branching fractions, the average energies removed by the antineutrinos and neutrinos, and the energy deposited by these decays.

Beta decay involves transforming a quark state in the nucleus and emission of a pair of fermions ($e^-\bar{\nu_e}$ or $e^+\nu_e$), where each fermion has an intrinsic angular momentum (or "spin") of 1/2. The decay satisfies all the relevant conservation principles of particle physics, including the electron-lepton number (L_e) conservation, where $L_e = 1$ for matter particles (e^-, ν_e) and $L_e = -1$ for antimatter particles ($e^+, \bar{\nu_e}$). The transformation is accompanied by a change in the total angular momentum of the nucleus (ΔI) which, by conservation of angular momentum, must be reflected in the state of the $e\nu$ pair, that is, the total orbital angular momentum (L) and the total spin angular momentum (S^L) of the $e\nu$ pair. Beta decays can be pure Fermi transitions, pure Gamow-Teller

transitions, or a combination of both. In Fermi transitions the spins of the emitted leptons are anti-parallel, $S^L = 0$, and therefore ΔI is matched only by $\pm L$. In Gamow-Teller transitions the spins of the emitted leptons are aligned, i.e., $S^L = 1$, and coupled to the change in nuclear angular momentum state ΔI together with L: $\Delta I = \pm|L \pm 1|$. The so-called "unique" transitions are Gamow-Teller transitions where L and S^L are aligned, $\Delta I = \pm|L + 1|$. Typically, transitions with a higher L have a longer half-life ($t_{1/2}$), because of less overlap of the $e\nu$ wave functions with the nucleus. Transitions with a non-zero L are called "forbidden" (as opposed to "allowed" for $L = 0$), which really means suppressed decays that involve changes in nuclear spin state; in n-th forbidden transition the $e\nu$ pair carries n units of orbital angular momentum (Bielajew, 2014). For example, the ^{40}K decay scheme involves a third unique forbidden transition, whereas the ^{87}Rb decay scheme involves a third non-unique forbidden transition.

Following Fermi's theory and working in units $\hbar = m_e = c = 1$, the shape of a β spectrum is calculated from

$$\frac{dN}{dw} \propto pwq^2 F(Z, w) S(w) \tag{2}$$

and normalized to the branching fraction of the specific β decay (Enomoto, 2005). In equation (2) $w = 1+E$ is the total energy of the β-particle (E being its kinetic energy), $p = \sqrt{w^2 - 1}$ is the momentum of the β-particle, q is the total energy of the neutrino (equal to its momentum as the neutrino mass is negligible) satisfying $E+q = E_{\text{end}}$, where E_{end} is the endpoint energy of the transition (in the case of a transition to ground state, it is the Q-value), and Z is the charge of the daughter nucleus. The left-hand side of equation (2) is the probability of a β particle to be created with energy in the dw vicinity of w, where w goes from 1 to $1+E_{\text{end}}$. The right-hand side is a product of three factors, the phase space factor pwq^2, the Fermi function $F(Z, w)$, and the shape factor $S(w)$. The Fermi function

$$F(Z, w) \propto (w^2 - 1)^{\gamma - 1} \mathrm{e}^{\pi\eta} \left|\Gamma(\gamma + i\eta)\right|^2, \tag{3}$$

where

$$\gamma = \sqrt{1 - (\alpha Z)^2}, \tag{4}$$

$$\eta = \frac{\alpha Z w}{\sqrt{w^2 - 1}}, \tag{5}$$

α being the fine-structure constant, accounts for the Coulombic interaction between the daughter nucleus and the outgoing β-particle (Enomoto, 2005). The shape factor $S(w)$, often written at $S(p, q)$, is equal to 1 for allowed transitions and has a more complex energy-dependence in the case of forbidden transitions.

A review of many β^- decay energy spectra was recently given by Mougeot (2015), including the shape factors used for the forbidden transitions. We adopt these shape factors in our calculations, but also include additional β decays not studied by Mougeot (2015); the shape factors used here are listed in Table 4. We have performed the β spectra evaluation and calculated the average energy removed by the ν_e and $\bar{\nu_e}$, which are reported as Q_ν (MeV) in Table 3 and can be calculated from $Q - Q_h$ in Table 4.

3 Radiogenic heat and geoneutrino luminosity of the Earth

Using decay constants for short-lived and long-lived radionuclides and ^{40}K branching ratio from the geological literature we calculate the heat production and geoneutrino

luminosity of the bulk silicate Earth (BSE) based on a model composition (Tables 3 and 4 and references therein). Compositional models differ on the absolute amount of refractory elements (e.g., Ca and Al) in the Earth (see review in W. F. McDonough (2016)), which includes La, Sm, Lu, Re, Pt, Th, and U. The model composition for the BSE fixes the absolute abundances of the refractory elements at 2.75 times that in CI1 chondrites (W. F. McDonough & Sun, 1995). For critical volatile elements, there is a reasonable consensus for ratios with refractory elements. For example, Arevalo Jr. et al. (2009) reported the K/U value for the silicate Earth as $13,800 \pm 1,300$ (1 standard deviation). Constraints for Rb come from the constancy of the Ba/Rb and the Sr–Nd isotopic system (assumes the BSE has an $^{87}Sr/^{86}Sr$ between 0.7040 and 0.7060, based on the mantle array (Hofmann, 2007)) and the Rb/Sr values (Ba and Sr are refractory elements with abundances set at 2.75 times that in CI1 chondrites) for the bulk silicate Earth, leading to a Rb/Sr of 0.032 ± 0.007 (W. F. McDonough et al., 1992).

Heat production and geoneutrino emission data for ^{40}K, ^{87}Rb, ^{147}Sm, ^{232}Th, ^{235}U, and ^{238}U are reported in Table 3, as these are the most significant present-day producers within the Earth. In fact, 99.5 % of the Earth's radiogenic heat production comes from ^{40}K, ^{232}Th, ^{235}U, and ^{238}U alone. The fractional contributions to heat production from ^{138}La, ^{176}Lu, ^{187}Re, and ^{190}Pt add up to $< 3 \times 10^{-5}$ of the total radiogenic heat and 1 % of the Earth's geoneutrino luminosity, with virtually all of this latter minor contributions coming from ^{187}Re. Figure 2 illustrates the present day relative contributions of heat production and geoneutrino luminosity from the major radionuclides reported in Table 3.

A simple formula for the present-day radiogenic heating rate $\tilde{h}$ (in nanowatts per kilogram of rock) from long-lived radionuclides is presented in equation (6), where A is elemental concentration as mass fraction (kg-element/kg-rock; e.g., [K] is mass fraction of potassium), and the remaining parameters combine into numerical factors whose values are set (N_A is Avogadro's number, X is natural molar isotopic fraction, μ is molar mass of element, λ is decay constant, Q_h is radiogenic heat released per decay). Multiplying with the mass of the geochemical reservoir of interest M_{res} (to which the elemental concentrations apply), one gets the total radiogenic power H (in terawatts) in that reservoir as shown in equation (7). Similarly, the natural specific antineutrino and neutrino luminosities $\tilde{l}$ (in number of particles per second per kilogram of rock) are calculated from equations (8) and (9). Multiplication with a reservoir mass gives the total luminosities $L_{\bar{\nu}_e}$ and L_{ν_e} (equation 10; contributions from individual elements listed in Table 3).

$$\tilde{h}\ [\mathrm{nW\,kg^{-1}}] = \sum_{\text{LLRs}} \frac{N_A X \lambda Q_h}{\mu} A = 3.387\,[\mathrm{K}] + 11.39\,[\mathrm{Rb}] + 46.07\,[\mathrm{Sm}] + 26180\,[\mathrm{Th}] + 98293\,[\mathrm{U}] \quad (6)$$

$$H\ [\mathrm{TW}] = \tilde{h} \times M_{\text{res}} \times 10^{-21} \quad (7)$$

$$\tilde{l}_{\bar{\nu}_e}\ [\mathrm{s^{-1}\,kg^{-1}}] = \sum_{\text{LLRs}} \frac{N_A X \lambda n_{\bar{\nu}_e}}{\mu} A = (2.797\,[\mathrm{K}] + 86.82\,[\mathrm{Rb}] + 1617\,[\mathrm{Th}] + 7636\,[\mathrm{U}]) \times 10^4 \quad (8)$$

$$\tilde{l}_{\nu_e}\ [\mathrm{s^{-1}\,kg^{-1}}] = \sum_{\text{LLRs}} \frac{N_A X \lambda n_{\nu_e}}{\mu} A = 0.3302\,[\mathrm{K}] \times 10^4 \quad (9)$$

$$L\ [\mathrm{s^{-1}}] = \tilde{l} \times M_{\text{res}} \quad (10)$$

To understand the evolution of the Earth's radiogenic heat and geoneutrino luminosity we must understand the initial starting abundances of the SLR in the solar system (listed in Table 4). At 4.57 Ga the local interstellar medium was populated with gas-dust clouds that were likely in secular equilibrium with ambient galactic sources prior to solar system formation. Recent calculations by Wasserburg et al. (2017) demonstrate that the proportional inventory of ^{26}Al, ^{60}Fe, ^{107}Pd, and ^{182}Hf in the early solar system

is unlikely to be a product from an asymptotic giant branch (AGB) star. Moreover, supernova sources would likely provide abundant ^{26}Al and ^{60}Fe, whereas the early solar system content of ^{60}Fe is equivalent to the measly ambient galactic supply (Trappitsch et al., 2018). More recent suggestions envisage stellar winds from a massive Wolf-Rayet star injecting ^{26}Al to complement the local inventory of ambient galactic sources (Young, 2014; Gounelle, M. & Meynet, G., 2012; Dwarkadas et al., 2017). At the same time, the enhanced abundance of ^{53}Mn and the presence of very short half life isotopes (e.g., ^{41}Ca $t_{1/2} = 0.1$ Ma) present challenges to be explained by models invoking Wolf-Rayet stars (Vescovi et al., 2018). Thus, the addition of mass and momentum from such a stellar source could cause a gravitational collapse of a molecular gas-dust cloud, which may have triggered our solar system formation and explain the observed proportions of short-lived radionuclides.

The total heat production and geoneutrino luminosity for models of the BSE are plotted with respect to time in Figure 3, which were calculated using results from Tables 3 and 4 and updated values for the BSE (W. F. McDonough & Sun, 1995; Arevalo Jr. et al., 2009; Wipperfurth et al., 2018) and equations (6–10). This figure presents a simple illustrative example of the Earth's heat production and geoneutrino luminosity that assumes full mass at 1 million years after after solar system initiation.

The uncertainties for the BSE abundances reported in Table 3 are ±10 % for K and the refractory lithophile elements (Wipperfurth et al., 2018), with correlations between K, Th and U. Using this Earth model, the present day's fluxes are 19.9±3.0 TW (terawatts or 10^{12} watts) for radiogenic heat and the total geoneutrino luminosity is $(4.91 \pm 0.75) \times 10^{25}$ $(\bar{\nu_e} + \nu_e)$ s^{-1}. The results shown in Figure 3 are directly scalable for different size planetary bodies with a bulk Earth composition; lowering the mass of a planet by a factor of 10 results in a decease by a factor of 10 in the heat production and (anti)neutrino luminosity. The most important factors are the amount of refractory elements and the volatility curve for the planet. The Earth has an Fe/Al value of 20±2 (W. F. McDonough & Sun, 1995; Allègre et al., 1995), comparable to the chondritic ratio, which is 19 ± 4 (less the 35 value for EH chondrites). The Fe/Al value sets the proportion of refractory elements (Al) to one of the 4 major elements (i.e., O, Fe, Mg and Si) that make up $\sim$ 93 % of the mass of a terrestrial planet. These latter elements are not in fixed chondritic proportions, as is the case for the refractory elements, thus, the mass proportion of O, Fe, Si and Mg can be approximated as 30:30:20:20 (or 50:15:15:15 for atomic proportions), respectively, with proportional differences leading to variations in the metal/silicate mass fraction and fraction of olivine (Mg_2SiO_4) to pyroxene ($MgSiO_3$) in the silicate shell. A K/U or K/Th value sets the volatile depletion curve for the planet. Using $\tilde{h}/A$ factors given in Table 4 and equations (6) and (7), one can model the thermal history of various size bodies in the solar system and exoplanets.

We can also compare these results for the present-day radiogenic power and geoneutrino flux versus that reported in the literature. In our comparison and where possible, we used the abundances and masses reported in Table 3 to carry out these comparisons. The calculated BSE radiogenic power in the models of Enomoto (2006a), Dye (2012), and Ruedas (2017) differs from our values by −0.2 %, 0.5 %, and 0.3 %, respectively. The antineutrino luminosity ($\bar{\nu_e}$ from K, Rb, Th and U) of the modeled BSE from this study and that calculated using the numbers in Enomoto (2006a), Dye (2012), and Usman et al. (2015) yields a 68 %, 67 %, and 25 % difference, respectively; we note that Dye (2012), and Usman et al. (2015) did not include ^{87}Rb in their calculations, which contributes 5 % of the flux.

4 Secular variation in the heat and luminosity of the Earth

Secular evolution of the Earth's heat production reveals that only two of the short-lived radionuclides, ^{26}Al, and ^{60}Fe, contribute any significant amount of additional heat-

ing to the accreting Earth above the power coming from the long-lived radionuclides (Figure 4). Formation and growth of the Earth is envisaged as a process that occurred on timescales of 10^7 years. Planetary growth initiated from planetesimal "seeds" that were 10^2 km in scale and likely formed contemporaneous with CAI (Calcium Aluminum Inclusion) formation at $t_{\text{zero}} = t_{\text{CAI}}$ (i.e., oldest known materials in the solar system) or shortly thereafter.

The inner solar system (circa inside of 4 AU), the domain of the terrestrial planets and rocky asteroids, has been characterized as home to the NC meteorites, the non-carbonaceous meteorites (Warren, 2011). Recent findings from various isotope studies of iron meteorites (Kruijer et al., 2017, 2014; Hilton et al., 2019) show that many of these "NC" bodies formed contemporaneous with t_{CAI} or up to 3 million years after t_{CAI} formation. It is generally concluded that the larger of these early formed planetesimals rapidly grew in a runaway growth phase followed by oligarchic growth to where they reach Mars and Mercury size bodies, however, if the growth process also included pebble accretion it can occur faster (Izidoro & Raymond, 2018; Johansen & Lambrechts, 2017).

The mean timescales τ for terrestrial planet formation (corresponding to accretion of $\sim$63 % of the planet's mass according to planetary mass growth parameterization $M(t)/M_{\text{final}} = 1-\exp(-t/\tau)$) are not well constrained. Mars is suggested to have τ of $\sim$2 million years after t_{CAI}, coincident with core formation (Dauphas & Pourmand, 2011; Tang & Dauphas, 2014), meaning it likely formed within the lifetime of the protoplanetary disk. Formation timescales also depend on position in the disk (Johansen & Lambrechts, 2017). Izidoro & Raymond (2018) found, depending on the particular growth regime assumed in a model of oligarchic growth and the role of gravitational focusing, that there is up to two orders of magnitude difference in the timescale of accretion at 1 AU.

The characteristic accretion time for the Earth is recognized as a significant unknown. We calculated a series of plausible growth curves in Figure 4 (inset) assuming the exponential growth function. With $\tau = 10$ Myr (red curve), the Earth is virtually fully ($> 99\%$) accreted at $\sim$ 50 million years after t_{CAI}, approximately at a plausible timing for a putative *Giant impact* event that lead to Moon formation (Barboni et al., 2017; Hosono et al., 2019).

The calculated radiogenic power of the Earth is plotted as a function of accretion time (Figure 4). The peak radiogenic heating occurs at about 1 to 5 million years after t_{CAI}, equivalent to the time scale for Mars accretion, when the proto-Earth produces 5×10^3 to 5×10^4 TW of power, mostly from the decay of ^{26}Al. This power is added on top of the kinetic energy deposited by impacts during accretion.

Some core formation models, particularly those invoking continuous metal-silicate segregation, suggest a mean age of core separation of $\sim$10 million years after t_{CAI} (Kleine et al., 2009). At this time the combined heat production from ^{26}Al and ^{60}Fe accounts for $\sim$90 % of the $\sim$300 TW of radiogenic power in the Earth. Between 10 and 15 million years after t_{CAI}, heat production from ^{60}Fe exceeds that of ^{26}Al and the long-lived radionuclides, despite the recent low estimate for the initial $(^{60}\text{Fe}/^{56}\text{Fe})_i$ of $(3.8\pm6.9)\times10^{-8}$ (Trappitsch et al., 2018). These findings leave little doubt as to the early hot start of the Earth and the likely melting temperatures experienced by both the forming Fe-rich core and surrounding silicate mantle. Moreover, isolating $\geq$90% of the Earth's iron into the core at this time results in a super-heated condition, given contributions from radiogenic, impact, and differentiation sources.

Figure 5 presents the heat production for two different bulk compositional models of small terrestrial planets (or asteroidal body). One model assume a bulk Earth-like composition (W. McDonough, 2014) with an Fe/Al = 20 and depletions in moderately volatile elements, while the other model assumes the same composition, except with moderately volatile elements set by a CI chondrite K/U value of 69,000 (Barrat et al., 2012).

A small difference in heat production for these two models in the first 15 million years of solar system history is revealed.

The potential of melting of a small body accreted in the first 2 million years of solar system history depends on its specific power h in W/kg, where h compares to $C_P\Delta T/\Delta t$, giving us the temperature increase of a body due to its radiogenic heating of ΔT over a time period of Δt. For a 100 km radius body (i.e., a size commensurate with estimates of some parent bodies of iron meteorites (Goldstein et al., 2009)), a τ of 0.5 to 1 million years, and 100 nW/kg of average specific radiogenic heating $\tilde{h}$ (note the present-day value for bulk Earth in 3 pW/kg) would increase the body's temperature by some 3000 K (ΔT) in 1 million years (Δt), according to a simple balance $\tilde{h} = C_P\Delta T/\Delta t$, where C_P is specific heat. This temperature increase is sufficient to induce melting and enhance the effectiveness of metal-silicate fractionation, although the actual thermal evolution also depends on the ability of the growing body to get rid of its heat, and therefore its growth curve of accretion (Šrámek et al., 2012). With a 100 km radius body, one would expect molten core and mantle (Kleine et al., 2009).

5 Geoneutrino flux vs. radiogenic power

There is a positive correlation between the Earth's radiogenic power and its geoneutrino flux, with the former given in TW and the latter given in number of (anti)neutrinos per cm^2 per second ($cm^{-2}\,s^{-1}$). Measurements of geoneutrino signal can therefore place limits on the amount of Earth's radiogenic power, or Th and U abundance, and consequently constrain other refractory lithophile element concentrations (e.g., W. F. McDonough, 2017). The Earth's geoneutrino signal is often reported in units of TNU, which stands for terrestrial neutrino units, and is the number of geoneutrinos counted over a 1-year exposure in an inverse beta decay detector having 10^{32} free protons ($\sim$1 kiloton detector of liquid scintillation oil) and 100% detection efficiency. The conversion factor between signal in TNU and flux in $cm^{-2}\,\mu s^{-1}$ depends on the Th/U ratio and has a value of $0.11\,cm^{-2}\,\mu s^{-1}\,TNU^{-1}$ for Earth's $(Th/U)_{mass}$ of 3.8.

The Borexino experiment reported the geoneutrino signal (Agostini et al., 2015), based on a fixed $(Th/U)_{molar} = 3.9$. We conducted a Monte Carlo simulation to determine the total signal at the Borexino experiment, based on a reference lithospheric model for the local and global contributions to the total flux Wipperfurth et al. (2019). We assumed the following architecture of the BSE: lithosphere underlain by the Depleted Mantle (source of mid-ocean ridge basalt, MORB), with an underlying Enriched Mantle (source of ocean island basalts, OIB) and the volume fraction of Depleted Mantle to Enriched Mantle is 5:1 Arevalo et al. (2013). Input assumption for the MC simulation include: (1) U abundance in the BSE (6 to 40 ng/g), (2) BSE $(Th/U)_{mass}$ ($3.776^{+0.122}_{-0.075}$; Wipperfurth et al. (2018)) and $(K/U)_{mass}$ ($13,800\pm1,300$; Arevalo Jr. et al. (2009)), and (3) accept results with abundances of $U_{\text{Depleted Mantle}} \leq U_{\text{Enriched Mantle}}$. Figure 6 shows the intersection of the MC model and the measured signal; the ensemble of acceptable BSE models includes the intersection of the best fit line (MC results) and the measurement field determined by the Borexino experiment (i.e., total power of 16 to 38 TW).

Wipperfurth et al. (2019) conducted a similar analysis to that above for the KamLAND signal. The KamLAND experiment recently reported their geoneutrino signal of $34.9^{+6.0}_{-5.4}$ Watanabe (2016), also based on a fixed $(Th/U)_{molar} = 3.9$. The observed ensemble of acceptable BSE models (i.e., intersection of the best fit line (MC results) and the measurement field) determined by the KamLAND experiment is between 16 and 25 TW. A combined KamLAND and Borexino result favors a medium-H Earth model with moderate radiogenic power.

Acknowledgments

WFM gratefully acknowledges NSF support (EAR1650365), SAW acknowledges support from NSF (EAPSI #1713230) and Japanese Society for the Promotion of Science (SP17054), and OŠ acknowledges Czech Science Foundation support (GAČR 17-01464S) for this research. We thank the many geo-, nuclear, and particle physics friends who have helped us to understand many of the details of these calculations, especially, Béda Roskovec, Steve Dye, John Learned, Sanshiro Enomoto, Hiroko Watanabe, Katherine Bermingham, and Richard Ash.

Data availability

The calculations performed in this study are openly available in the form of a Jupyter Notebook in 4TU.ResearchData repository at `https://doi.org/10.4121/uuid:191c7802-8835-4791-9c2d-31426dcb5d15`.

Authors contribution

WFM, SAW, and OŠ proposed and conceived of various portions of this study and also independently conducted heat production and luminosity calculations. OŠ calculated the β decay spectra for the SLR and ^{40}K. All authors contributed to the interpretation of the results. The manuscript was written by WFM, with edits and additions from OŠ, and SAW. All authors read and approved of the final manuscript.

References

Agostini, M., Appel, S., Bellini, G., Benziger, J., Bick, D., Bonfini, G., ... others (2015). Spectroscopy of geoneutrinos from 2056 days of Borexino data. *Physical Review D*, *92*(3), 031101. doi: https://doi.org/10.1103/PhysRevD.92.031101

Allègre, C. J., Poirier, J.-P., Humler, E., & Hofmann, A. W. (1995). The chemical composition of the earth. *Earth and Planetary Science Letters*, *134*(3), 515 - 526. doi: https://doi.org/10.1016/0012-821X(95)00123-T

Arevalo, R., McDonough, W. F., Stracke, A., Willbold, M., Ireland, T. J., & Walker, R. J. (2013). Simplified mantle architecture and distribution of radiogenic power. *Geochemistry, Geophysics, Geosystems*, *14*(7), 2265–2285.

Arevalo Jr., R., McDonough, W. F., & Luong, M. (2009). The K/U ratio of the silicate Earth: Insights into mantle composition, structure and thermal evolution. *Earth and Planetary Science Letters*, *278*(3-4), 361–369. doi: 10.1016/j.epsl.2008.12.023

Baker, R. G. A., Schonbachler, M., Rehkamper, M., Williams, H. M., & Halliday, A. N. (2010). The thallium isotope composition of carbonaceous chondrites — New evidence for live ^{205}Pb in the early solar system. *Earth and Planetary Science Letters*, *291*(1-4), 39-47. doi: 10.1016/J.EPSL.2009.12.044

Barboni, M., Boehnke, P., Keller, B., Kohl, I. E., Schoene, B., Young, E. D., & McKeegan, K. D. (2017). Early formation of the moon 4.51 billion years ago. *Science Advances*, *3*(1). doi: 10.1126/sciadv.1602365

Barrat, J.-A., Zanda, B., Moynier, F., Bollinger, C., Liorzou, C., & Bayon, G. (2012). Geochemistry of ci chondrites: Major and trace elements, and cu and zn isotopes. *Geochimica et Cosmochimica Acta*, *83*, 79–92.

Becker, H., & Walker, R. J. (2003). Efficient mixing of the solar nebula from uniform Mo isotopic composition of meteorites. *Nature*, *425*(6954), 152–155. doi: 10.1038/nature01975

Begemann, F., Ludwig, K. R., Lugmair, G. W., Min, K., Nyquist, L. E., Patchett, P. J., ... Walker, R. J. (2001). Call for an improved set of decay constants for geochronological use. *Geochimica et Cosmochimica Acta*, *65*(1), 111–121. doi:

10.1016/S0016-7037(00)00512-3

Bermingham, K. R., Mezger, K., Desch, S. J., Scherer, E. E., & Horstmann, M. (2014). Evidence for extinct ^{135}Cs from Ba isotopes in Allende CAIs? *Geochimica et Cosmochimica Acta*, *133*, 463–478. doi: 10.1016/J.GCA.2013.12.016

Bielajew, A. F. (2014, December). Introduction to special relativity, quantum mechanics and nuclear physics for nuclear engineers [Computer software manual]. Retrieved from `http://www.umich.edu/~ners311/CourseLibrary/bookchapter15.pdf` (Chapter 15 (NERS 311/312: Elements of Nuclear Engineering and Radiological Sciences I/II, Reading and Supplementary Material/Fall 2014/Winter 2015))

Bouvier, L. C., Costa, M. M., Connelly, J. N., Jensen, N. K., Wielandt, D., Storey, M., ... Bizzarro, M. (2018). Evidence for extremely rapid magma ocean crystallization and crust formation on mars. *Nature*, *558*(7711), 586-589. doi: 10.1038/s41586-018-0222-z

Braun, M., Georgiev, Y. M., Schönherr, T., Wilsenach, H., & Zuber, K. (2017). A new precision measurement of the α-decay half-life of ^{190}Pt. *Physics Letters B*, *768*, 317–320. doi: 10.1016/j.physletb.2017.02.052

Brennecka, G. A., Borg, L. E., Romaniello, S. J., Souders, A. K., Shollenberger, Q. R., Marks, N. E., & Wadhwa, M. (2017). A renewed search for short-lived ^{126}Sn in the early Solar System: Hydride generation MC-ICPMS for high sensitivity Te isotopic analysis. *Geochimica et Cosmochimica Acta*, *201*, 331–344. doi: 10.1016/j.gca.2016.10.003

Chen, J. (2017). Nuclear data sheets for $A = 40$. *Nuclear Data Sheets*, *140*, 1–376. doi: 10.1016/j.nds.2017.02.001

Cook, D. L., Walker, R. J., Horan, M. F., Wasson, J. T., & Morgan, J. W. (2004). Pt-Re-Os systematics of group IIAB and IIIAB iron meteorites. *Geochimica et Cosmochimica Acta*, *68*(6), 1413–1431. doi: 10.1016/j.gca.2003.09.017

Dauphas, N., & Pourmand, A. (2011). Hf-w-th evidence for rapid growth of mars and its status as a planetary embryo. *Nature*, *473*, 489 EP -. doi: 10.1038/nature10077

Dauphas, N., Rauscher, T., Marty, B., & Reisberg, L. (2003). Short-lived p-nuclides in the early solar system and implications on the nucleosynthetic role of X-ray binaries. *Nuclear Physics A*, *719*, C287–C295. doi: 10.1016/S0375-9474(03)00934-5

Dwarkadas, V. V., Dauphas, N., Meyer, B., Boyajian, P., & Bojazi, M. (2017). Triggered star formation inside the shell of a wolf–rayet bubble as the origin of the solar system. *The Astrophysical Journal*, *851*(2), 147.

Dye, S. T. (2012). Geoneutrinos and the radioactive power of the Earth. *Reviews of Geophysics*, *50*(3). doi: 10.1029/2012RG000400

Enomoto, S. (2005). *Neutrino geophysics and observation of geo-neutrinos at KamLAND* (Doctoral dissertation, Tohoku University). Retrieved from `http://kamland.lbl.gov/research-projects/kamland/student-dissertations/EnomotoSanshiro-DoctorThesis.pdf`

Enomoto, S. (2006a). Experimental study of geoneutrinos with KamLAND. *Earth Moon and Planets*, *99*(1-4), 131–146.

Enomoto, S. (2006b). *Geoneutrino spectrum and luminosity.* Retrieved 2006, from `http://www.awa.tohoku.ac.jp/~sanshiro/research/geoneutrino/spectrum/`

Farley, T. A. (1960). Half-period of th232. *Canadian Journal of Physics*, *38*(8), 1059-1068. doi: 10.1139/p60-114

Fiorentini, G., Lissia, M., & Mantovani, F. (2007). Geo-neutrinos and earth's interior. *Physics Reports*, *453*(5-6), 117–172. doi: 10.1016/j.physrep.2007.09.001

Gilmour, J. D., & Crowther, S. A. (2017). The I-Xe chronometer and its constraints on the accretion and evolution of planetesimals. *Geochemical Journal*, *51*(1), 69–80. doi: 10.2343/geochemj.2.0429

Goldstein, J., Scott, E., & Chabot, N. (2009). Iron meteorites: Crystallization, thermal history, parent bodies, and origin. *Chemie der Erde - Geochemistry*, *69*(4), 293 - 325. doi: https://doi.org/10.1016/j.chemer.2009.01.002

Gounelle, M., & Meynet, G. (2012). Solar system genealogy revealed by extinct short-lived radionuclides in meteorites. *A&A*, *545*, A4. doi: 10.1051/0004-6361/201219031

Hiess, J., Condon, D. J., McLean, N., & Noble, S. R. (2012). $^{238}U/^{235}U$ systematics in terrestrial uranium-bearing minerals. *Science (New York, N.Y.)*, *335*(6076), 1610–4. doi: 10.1126/science.1215507

Hilton, C. D., Bermingham, K. R., Walker, R. J., & McCoy, T. J. (2019). Genetics, crystallization sequence, and age of the south byron trio iron meteorites: New insights to carbonaceous chondrite (cc) type parent bodies. *Geochimica et Cosmochimica Acta*, *251*, 217–228.

Hofmann, A. W. (2007). Sampling mantle heterogeneity through oceanic basalts: Isotopes and trace elements. In *Treatise on geochemistry* (pp. 1–44). Elsevier.

Hosono, N., Karato, S.-i., Makino, J., & Saitoh, T. R. (2019). Terrestrial magma ocean origin of the moon. *Nature Geoscience*, 1.

Iizuka, T., Lai, Y.-J., Akram, W., Amelin, Y., & Schonbachler, M. (2016). The initial abundance and distribution of ^{92}Nb in the Solar System. *Earth and Planetary Science Letters*, *439*, 172–181. doi: 10.1016/J.EPSL.2016.02.005

Izidoro, A., & Raymond, S. N. (2018). Formation of terrestrial planets. In H. J. Deeg & J. A. Belmonte (Eds.), *Handbook of exoplanets* (pp. 1–59). Cham: Springer International Publishing. doi: 10.1007/978-3-319-30648-3_142-1

Jaffey, A. H., Flynn, K. F., Glendenin, L. E., Bentley, W. C., & Essling, A. M. (1971). Precision measurement of half-lives and specific activities of ^{235}U and ^{238}U. *Physical Review C*, *4*(5), 1889–1906. doi: 10.1103/PhysRevC.4.1889

Johansen, A., & Lambrechts, M. (2017). Forming planets via pebble accretion. *Annual Review of Earth and Planetary Sciences*, *45*(1), 359-387. doi: 10.1146/annurev-earth-063016-020226

Kita, N. T., Yin, Q.-Z., MacPherson, G. J., Ushikubo, T., Jacobsen, B., Nagashima, K., ... Jacobsen, S. B. (2013). ^{26}Al-^{26}Mg isotope systematics of the first solids in the early solar system. *Meteoritics & Planetary Science*, *48*(8), 1383-1400. doi: 10.1111/maps.12141

Kleine, T., Touboul, M., Bourdon, B., Nimmo, F., Mezger, K., Palme, H., ... Halliday, A. N. (2009). Hf–W chronology of the accretion and early evolution of asteroids and terrestrial planets. *Geochimica et Cosmochimica Acta*, *73*(17), 5150 - 5188. (The Chronology of Meteorites and the Early Solar System) doi: 10.1016/j.gca.2008.11.047

Kruijer, T. S., Burkhardt, C., Budde, G., & Kleine, T. (2017). Age of jupiter inferred from the distinct genetics and formation times of meteorites. *Proceedings of the National Academy of Sciences*, *114*(26), 6712–6716. doi: 10.1073/pnas.1704461114

Kruijer, T. S., Kleine, T., Fischer-Gödde, M., Burkhardt, C., & Wieler, R. (2014). Nucleosynthetic W isotope anomalies and the Hf–W chronometry of Ca–Al-rich inclusions. *Earth and Planetary Science Letters*, *403*, 317–327. doi: 10.1016/j.epsl.2014.07.003

Leutz, H., Schulz, G., & Wenninger, H. (1965, 01). The decay of potassium-40. *Zeitschrift für Physik*, *187*(2), 151–164. doi: 10.1007/BF01387190

Liu, M.-C. (2017). The initial $^{41}Ca/^{40}Ca$ ratios in two type A Ca–Al-rich inclusions: Implications for the origin of short-lived ^{41}Ca. *Geochimica et Cosmochimica Acta*, *201*, 123–135. doi: 10.1016/j.gca.2016.10.011

Liu, M.-C., Nittler, L. R., Alexander, C. M. O., & Lee, T. (2010). Lithium-beryllium-boron isotopic compositions in meteoritic hibonite: implications for origin of ^{10}Be and early Solar System irradiation. *The Astrophysical Journal*,

719(1), L99–L103. doi: 10.1088/2041-8205/719/1/L99

Marks, N., Borg, L., Hutcheon, I., Jacobsen, B., & Clayton, R. (2014). Samarium–neodymium chronology and rubidium–strontium systematics of an allende calcium–aluminum-rich inclusion with implications for 146sm half-life. *Earth and Planetary Science Letters*, *405*, 15 - 24. doi: https://doi.org/10.1016/j.epsl.2014.08.017

Matthes, M., Fischer-Godde, M., Kruijer, T. S., & Kleine, T. (2017). Pd-Ag chronometry of IVA iron meteorites and the crystallization and cooling of a protoplanetary core. *Geochimica et Cosmochimica Acta*, *365*. doi: 10.1016/J.GCA.2017.09.009

McDonough, W. (2014). 3.16 - compositional model for the earth's core. In H. D. Holland & K. K. Turekian (Eds.), *Treatise on geochemistry (second edition)* (Second Edition ed., p. 559 - 577). Oxford: Elsevier.

McDonough, W. F. (2016). The composition of the lower mantle and core. In Hidenori Terasaki & Rebecca A. Fischer (Eds.), *Deep earth: Physics and chemistry of the lower mantle and core* (pp. 143–159). Washington DC: John Wiley & Sons, Inc.

McDonough, W. F. (2017). Geoneutrinos. In W. M. White (Ed.), *Encyclopedia of geochemistry: A comprehensive reference source on the chemistry of the earth* (p. 1-13). Springer International Publishing. doi: 10.1007/978-3-319-39193-9_213-1

McDonough, W. F., & Sun, S. S. (1995). The composition of the Earth. *Chemical Geology*, *120*(3-4), 223-253. doi: 10.1016/0009-2541(94)00140-4

McDonough, W. F., Sun, S. S., Ringwood, A. E., Jagoutz, E., & Hofmann, A. W. (1992). Potassium, rubidium, and cesium in the Earth and Moon and the evolution of the mantle of the Earth. *Geochimica et Cosmochimica Acta*, *56*(3), 1001–1012.

Meissner, F., Schmidt-Ott, W. D., & Ziegeler, L. (1987, 01). Half-life and α-ray energy of146sm. *Zeitschrift für Physik A Atomic Nuclei*, *327*(2), 171–174. doi: 10.1007/BF01292406

Mougeot, X. (2015). Reliability of usual assumptions in the calculation of β and ν spectra. *Physical Review C*, *91*(5), 055504. doi: 10.1103/PhysRevC.91.055504

Naumenko-Dèzes, M. O., Nägler, T. F., Mezger, K., & Villa, I. M. (2018). Constraining the ^{40}K decay constant with ^{87}Rb-^{87}Sr—^{40}K-^{40}Ca chronometer intercomparison. *Geochimica et Cosmochimica Acta*, *220*, 235-247. doi: https://doi.org/10.1016/j.gca.2017.09.041

Renne, P. R., Balco, G., Ludwig, K. R., Mundil, R., & Min, K. (2011). Response to the comment by W.H. Schwarz et al. on "Joint determination of ^{40}K decay constants and ^{40}Ar/^{40}K for the Fish Canyon sanidine standard, and improved accuracy for ^{40}Ar/^{39}K geochronology" by P.R. Renne et al. (2010). *Geochimica et Cosmochimica Acta*, *75*(17), 5097–5100. doi: 10.1016/j.gca.2011.06.021

Ruedas, T. (2017). Radioactive heat production of six geologically important nuclides. *Geochemistry, Geophysics, Geosystems*. doi: 10.1002/2017GC006997

Sato, J., & Hirose, T. (1981). Half-life of ^{138}La. *Radiochemical and Radioanalytical Letters*, *46*, 145-152. doi: ISSN0079-9483

Söderlund, U., Patchett, P. J., Vervoort, J. D., & Isachsen, C. E. (2004). The ^{176}Lu decay constant determined by Lu-Hf and U-Pb isotope systematics of Precambrian mafic intrusions. *Earth and Planetary Science Letters*, *219*(3-4), 311–324. doi: 10.1016/S0012-821X(04)00012-3

Šrámek, O., Milelli, L., Ricard, Y., & Labrosse, S. (2012). Thermal evolution and differentiation of planetesimals and planetary embryos. *Icarus*, *217*(1), 339-354. doi: 10.1016/j.icarus.2011.11.021

Tang, H., & Dauphas, N. (2014). 60fe–60ni chronology of core formation in mars. *Earth and Planetary Science Letters*, *390*, 264 - 274. doi: https://doi.org/

10.1016/j.epsl.2014.01.005

Tanimizu, M. (2000). Geophysical determination of the ^{138}La β^- decay constant. *Phys. Rev. C*, *62*, 017601. doi: 10.1103/PhysRevC.62.017601

Trappitsch, R., Boehnke, P., Stephan, T., Telus, M., Savina, M. R., Pardo, O., ... Huss, G. R. (2018). New constraints on the abundance of ^{60}Fe in the early Solar System. *The Astrophysical Journal Letters*, *857*(2), L15.

Trinquier, A., Birck, J. L., Allègre, C. J., Göpel, C., & Ulfbeck, D. (2008). ^{53}Mn-^{53}Cr systematics of the early Solar System revisited. *Geochimica et Cosmochimica Acta*, *72*(20), 5146–5163. doi: 10.1016/j.gca.2008.03.023

Turner, G., Busfield, A., Crowther, S. A., Harrison, M., Mojzsis, S., & Gilmour, J. (2007). Pu–Xe, U–Xe, U–Pb chronology and isotope systematics of ancient zircons from Western Australia. *Earth and Planetary Science Letters*(3-4), 491-499. doi: 10.1016/J.EPSL.2007.07.014

Turner, G., Crowther, S. A., Gilmour, J. D., Kelley, S. P., & Wasserburg, G. J. (2013). Short lived ^{36}Cl and its decay products ^{36}Ar and ^{36}S in the early solar system. *Geochimica et Cosmochimica Acta*, *123*, 358–367. doi: 10.1016/J.GCA.2013.06.022

Usman, S. M., Jocher, G. R., Dye, S. T., McDonough, W. F., & Learned, J. G. (2015). AGM2015: Antineutrino Global Map 2015. *Scientific Reports*, *5*(1), 13945. doi: 10.1038/srep13945

Vescovi, D., Busso, M., Palmerini, S., Trippella, O., Cristallo, S., Piersanti, L., ... Kratz, K.-L. (2018). On the origin of early solar system radioactivities: Problems with the asymptotic giant branch and massive star scenarios. *The Astrophysical Journal*, *863*(2), 115.

Villa, I. M., Bonardi, M. L., De Bièvre, P., Holden, N. E., & Renne, P. R. (2016). IUPAC-IUGS status report on the half-lives of ^{238}U, ^{235}U and ^{234}U. *Geochimica et Cosmochimica Acta*, *172*, 387–392. doi: 10.1016/j.gca.2015.10.011

Villa, I. M., De Bièvre, P., Holden, N. E., & Renne, P. R. (2015). IUPAC-IUGS recommendation on the half life of ^{87}Rb. *Geochimica et Cosmochimica Acta*, *164*, 382–385. doi: 10.1016/j.gca.2015.05.025

Wang, M., Audi, G., Kondev, F. G., Huang, W., Naimi, S., & Xu, X. (2017). The AME2016 atomic mass evaluation (I). Evaluation of input data; and adjustment procedures. *Chinese Physics C*, *41*(3), 030002. doi: 10.1088/1674-1137/41/3/030002

Warren, P. H. (2011). Stable-isotopic anomalies and the accretionary assemblage of the earth and mars: A subordinate role for carbonaceous chondrites. *Earth and Planetary Science Letters*, *311*(1-2), 93–100.

Wasserburg, G. J., Busso, M., Gallino, R., & Raiteri, C. M. (1994). Asymptotic Giant Branch stars as a source of short-lived radioactive nuclei in the solar nebula. *The Astrophysical Journal*, *424*, 412. doi: 10.1086/173899

Wasserburg, G. J., Karakas, A. I., & Lugaro, M. (2017). Intermediate-mass asymptotic giant branch stars and sources of 26al, 60fe, 107pd, and 182hf in the solar system. *The Astrophysical Journal*, *836*(1), 126.

Watanabe, H. (2016). *KamLAND, presentation at international workshop : Neutrino research and thermal evolution of the earth.* Retrieved 2016, from `http://www.tfc.tohoku.ac.jp/wp-content/uploads/2016/10/04_HirokoWatanabe_TFC2016.pdf`

Wipperfurth, S. A., Guo, M., Šrámek, O., & McDonough, W. F. (2018). Earth's chondritic Th/U: Negligible fractionation during accretion, core formation, and crust–mantle differentiation. *Earth Planet. Sci. Lett.*, *498*, 196-202. (arXiv:1801.05473) doi: 10.1016/j.epsl.2018.06.029

Wipperfurth, S. A., Šrámek, O., & McDonough, W. F. (2019). *Reference models for lithospheric geoneutrino signal.* (submitted to Journal of Geophysical Research)

Young, E. D. (2014). Inheritance of solar short- and long-lived radionuclides from

molecular clouds and the unexceptional nature of the solar system. *Earth and Planetary Science Letters*, *392*, 16–27. doi: 10.1016/j.epsl.2014.02.014

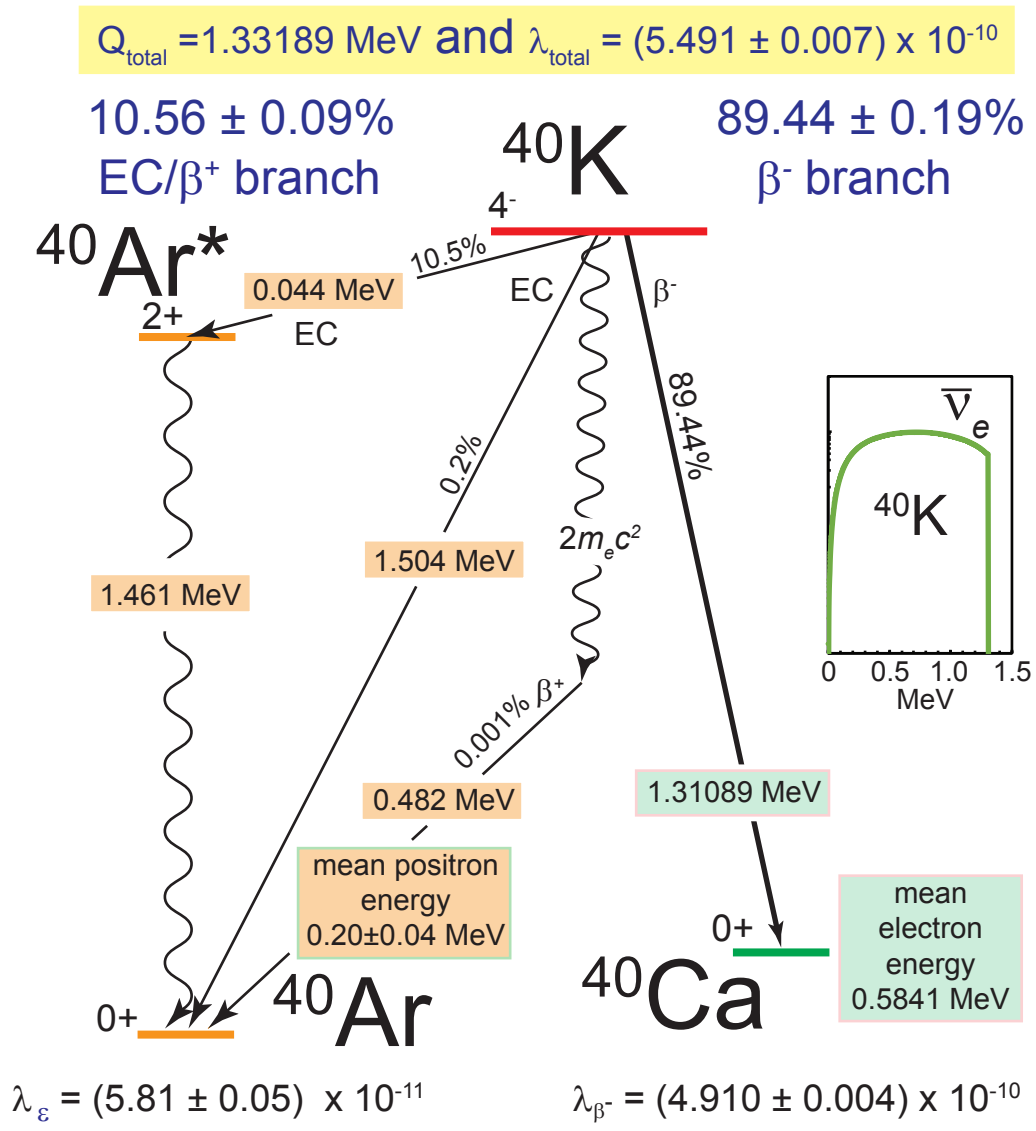

Figure 1. Decay scheme for ^{40}K. The beta-minus branch directly leads to ^{40}Ca in the ground state accompanied by the emission of an $\bar{\nu}_e$, whereas the electron capture branch has the emission of a 44 keV ν_e and an excited state of ^{40}Ar*, with the latter undergoing an isomeric transition to the ground state of ^{40}Ar via the emission of a 1.46 MeV γ-ray. Minor branches that we account for are electron capture and β^+ to ground state of ^{40}Ar. During β^- decay the energy is shared between the e^- and $\bar{\nu}_e$, with the latter particle removing on average 650 keV of energy from the Earth (accounting for branching; the mean $\bar{\nu}_e$ energy is 727 keV). Data for the branching ratios and the energies are from Chen (2017); Renne et al. (2011); Naumenko-Dèzes et al. (2018) and the antineutrino energy spectrum (with intensity in arbitrary units), shown in the inset, which uses the β^- shape factor from Leutz et al. (1965) to account for the correction of the third unique forbidden transition.

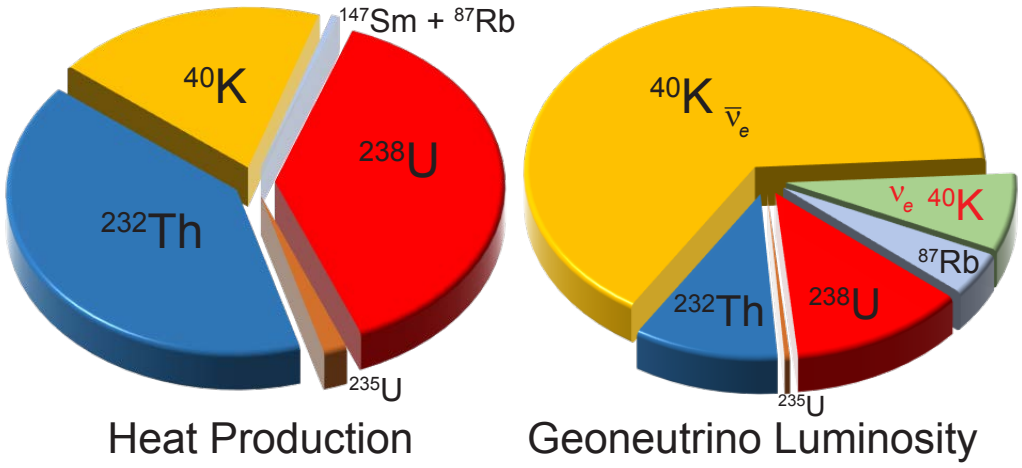

Figure 2. The relative contributions to radiogenic heat production and geoneutrino luminosity of the present-day Earth. Note the relative contributions of $\bar{\nu}_e$ and ν_e from ^{40}K in terms of geoneutrino luminosity. (Antineutrinos emitted by human-made nuclear reactors are not considered.)

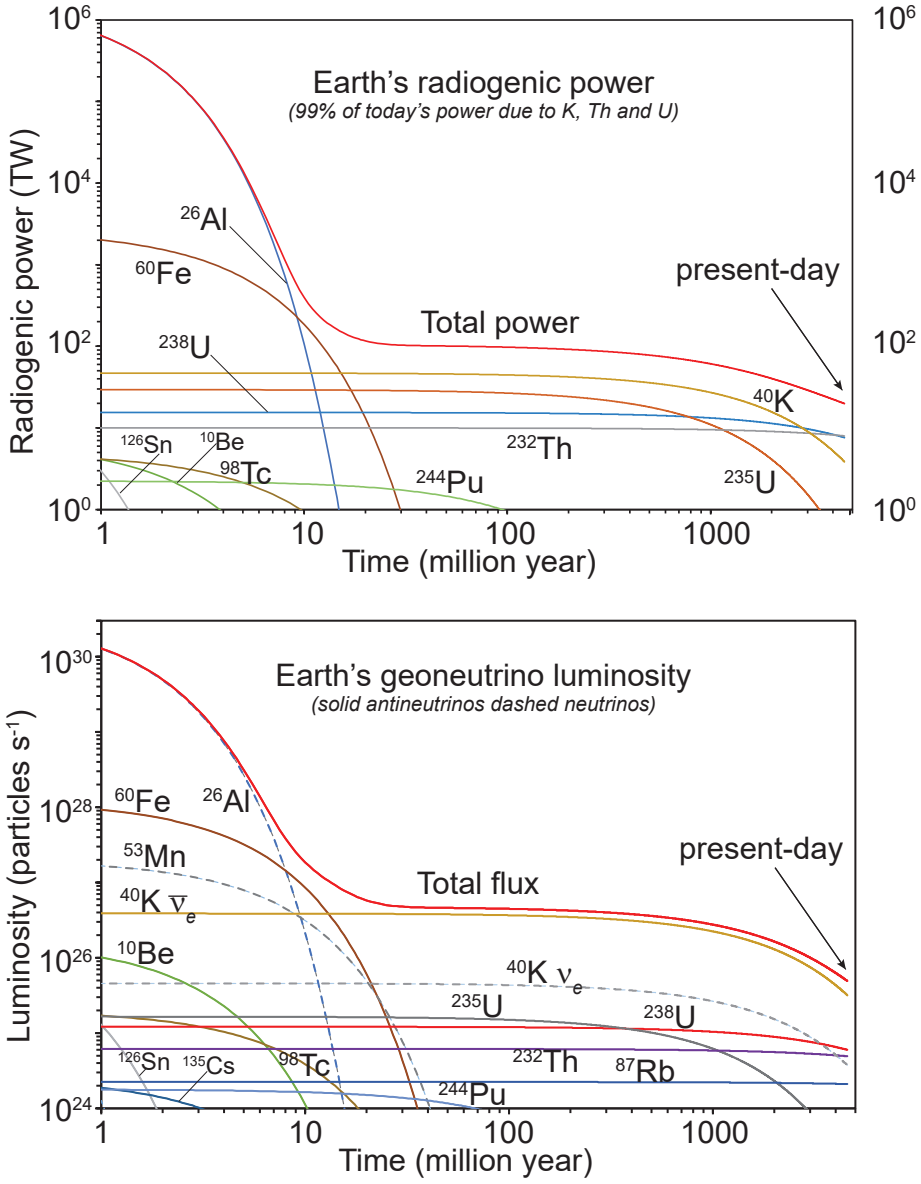

Figure 3. The Earth's radiogenic power (upper panel) and geoneutrino flux (lower panel) over the last 4568 million years. These figures assume an Earth mass of $\mathbf{6 \times 10^{24}}$ kg at all times. The power and geoneutrino flux is scalable; if one assumes 1/10 the planetary mass, it has 1/10 the power and luminosity, for an Earth bulk composition.

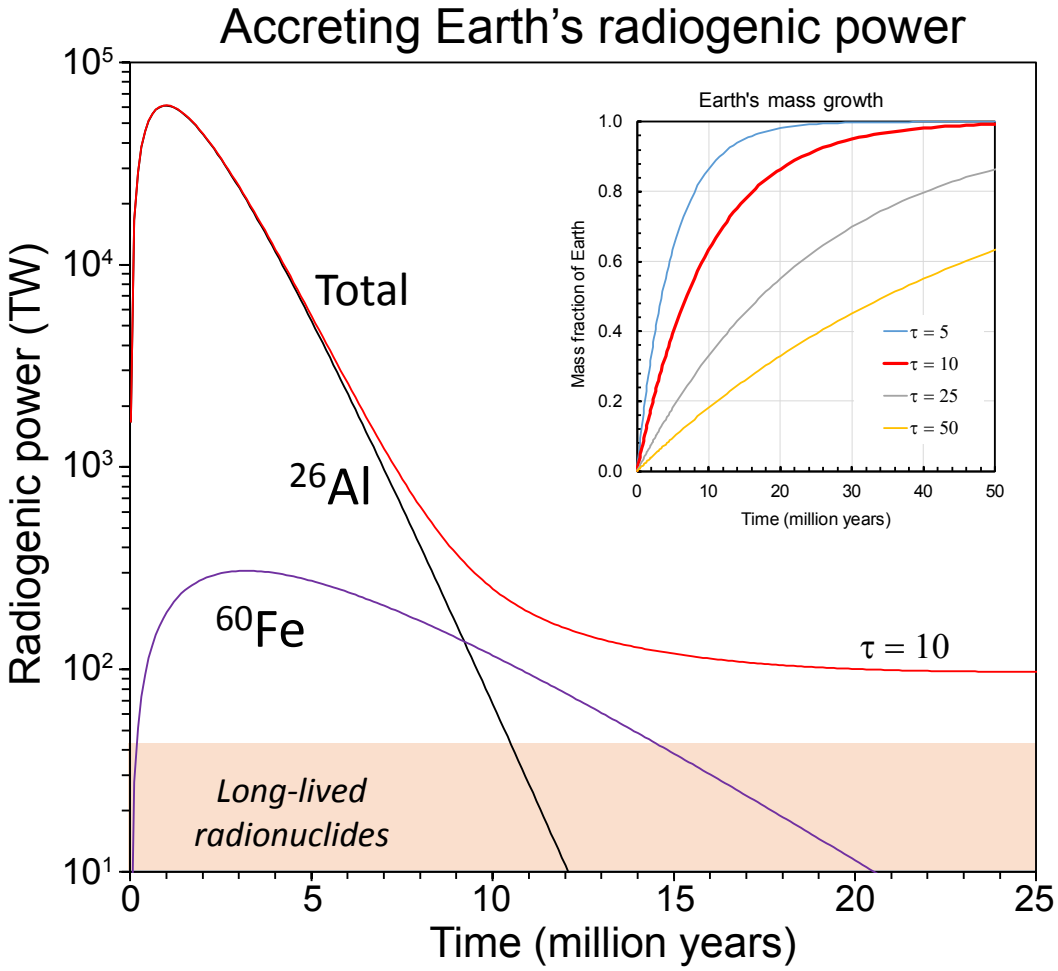

Figure 4. A plot of the relative contributions of radiogenic heat to the Earth during accretion over the first 25 million years of Solar system history. The long-lived radionuclides include: ^{40}K, ^{232}Th, ^{235}U, and ^{238}U. Figure 3 shows that other short-lived radionuclides contribute negligible amounts of power than what is shown here. Inset diagram shows a series of exponential growth curves $\boldsymbol{M(t)/M_{\text{final}} = 1 - \exp(-t/\tau)}$ for planets. Given an age of Mars of between 2 and 5 million years (Dauphas & Pourmand, 2011; Bouvier et al., 2018), its accretion history can be modeled assuming $\boldsymbol{\tau \leq 5}$. For the Earth we assume $\boldsymbol{\tau = 10}$, however the absolute $\boldsymbol{\tau}$ value is not significant, as there is only a 40% reduction in radiogenic power at the peak between a Mars and Earth accretion model.

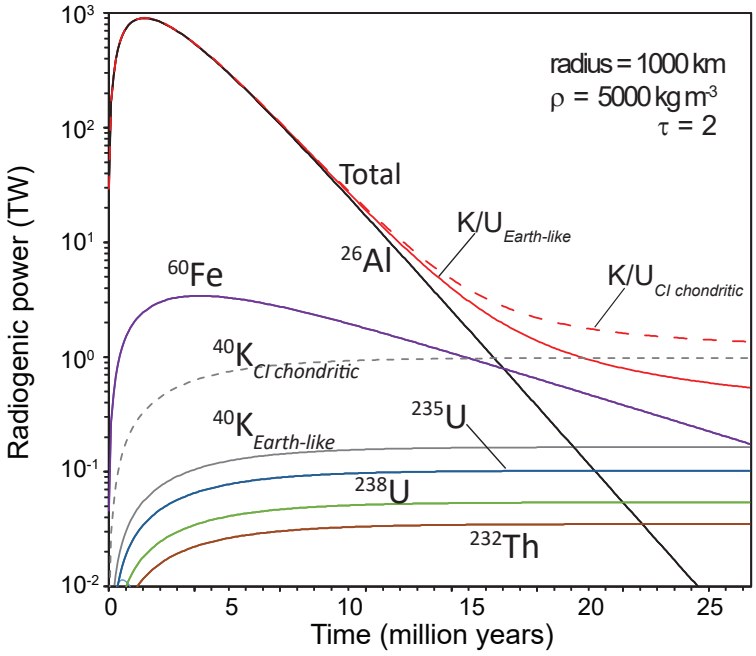

Figure 5. A plot of the relative contributions of radiogenic heat to a model terrestrial body (i.e., planet or asteroid) during accretion over the first 25 million years of solar system history. [In the bottom-most left corner of the plot is a tiny dark green peak from SRL ^{126}Sn, which provides a perspective for heat production from all of the remaining contributors.] Two model compositions are shown for K/U = 14,000 (Earth-like, solid lines) and K/U = 69,000 (CI chondrite, dashed lines); both models assume refractory elements at about 2 times that in CI chondrite, which is equivalent to an Earth-like water and CO_2 budget. The terrestrial body is modeled as having a τ value of 2 and a density of 5,000 kg/m^3. The left y-axis (radiogenic power) is for a body with a 100 km radius. The radiogenic power scales with the body size (assuming the same composition and density); for example, for a body with 1/10 of radius, hence 1/1000 of volume, the radiogenic power will be 3 orders of magnitude smaller.

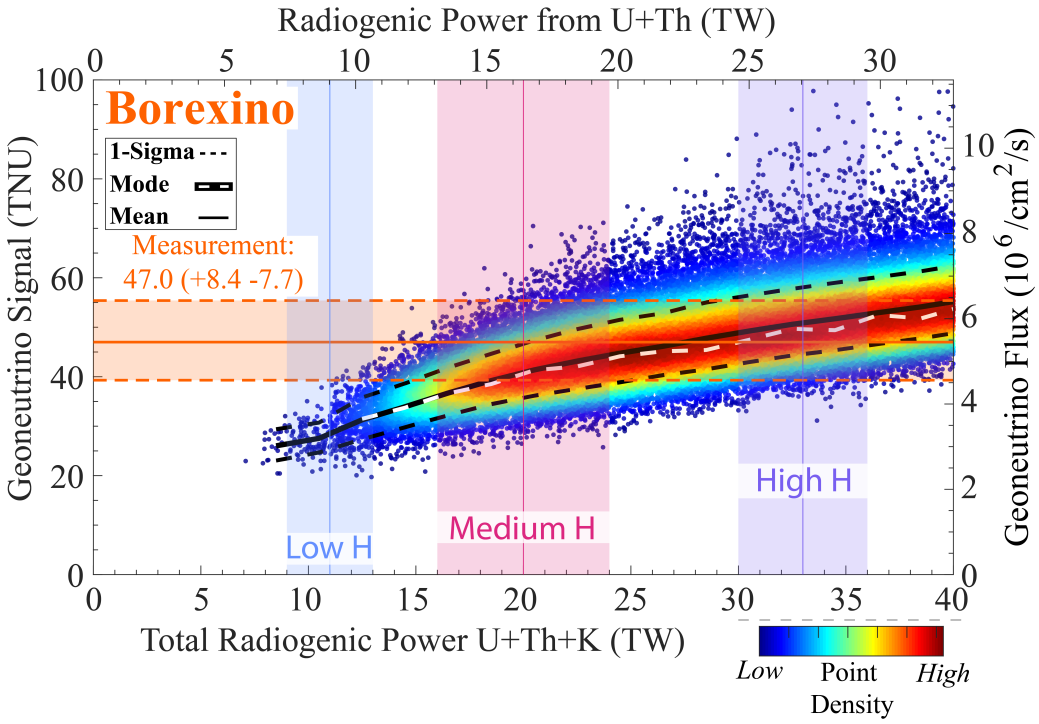

Figure 6. The TNU signal (left y-axis) or geoneutrino flux (in cm^{-2} s^{-1}; right y-axis) for the Borexino experiment versus the total radiogenic power (bottom x-axis) or only radiogenic power from Th + U (upper x-axis)(in TW) within the modeled BSE. The sloped array of points are the predictions generated with a Monte Carlo model using a reference lithosphere of the local and global contributions to the total geoneutrino flux for the Borexino location Wipperfurth et al. (2019). The minimum solution (leftmost points) is set by the $\mathbf{8.1^{+2.7}_{-2.0}}$ TW continental lithospheric model and negligible radiogenic power in the mantle. Measured data reported by the Borexino experiment (horizontal red band) is from Agostini et al. (2015). The low-H (blue), medium-H (pink), and high-H (purple) bands represent predictions of the BSE heat production. The 1-sigma, mean, and mode are calculated in bins every two TW.

Table 1. Extant long-lived radioactive decay systems

Decay system	Mole frac. (%)	Decay mode	λ (yr^{-1})	Q (MeV)
$^{40}K \rightarrow {}^{40}Ar$	0.01167	ε (10.56%)	5.810×10^{-11}	1.504
$^{40}K \rightarrow {}^{40}Ca$	0.01167	β^- (89.44%)	4.910×10^{-10}	1.311
^{40}K overall			5.491×10^{-10}	(total) 1.331
$^{87}Rb \rightarrow {}^{87}Sr$	27.83	β^-	1.397×10^{-11}	0.2823
$^{138}La \rightarrow {}^{138}Ce$	0.0888	β^- (34.8%)	2.34×10^{-12}	1.052
$^{138}La \rightarrow {}^{138}Ba$	0.0888	EC (65.2%)	4.39×10^{-12}	1.742
^{138}La overall			6.73×10^{-12}	(total) 1.504
$^{147}Sm \rightarrow {}^{143}Nd$	14.993	α	6.539×10^{-12}	2.311
$^{176}Lu \rightarrow {}^{176}Hf$	2.598	β^-	1.867×10^{-11}	1.194
$^{187}Re \rightarrow {}^{187}Os$	62.60	β^-	1.666×10^{-11}	0.0025
$^{190}Pt \rightarrow {}^{186}Os$	0.0136	α	1.415×10^{-12}	3.269
$^{232}Th \rightarrow {}^{208}Pb$	100	6α and $4\beta^-$	4.916×10^{-11}	(total) 42.646
$^{235}U \rightarrow {}^{207}Pb$	0.72033	7α and $4\beta^-$	9.8531×10^{-10}	(total) 46.397
$^{238}U \rightarrow {}^{206}Pb$	99.274	8α and $6\beta^-$	1.5513×10^{-10}	(total) 51.694

Decay energy Q calculated from mass differences between parent and final daughter nuclide mass data from Wang et al. (2017); see Table 2 for details on decay constant λ. ^{40}K and ^{138}La undergo branched decays; Q entries for ^{232}Th, ^{235}U, and ^{238}U account for the decay networks down to Pb nuclides. Mole fraction of U isotopes calculated from $U = {}^{238}U + {}^{235}U + {}^{234}U$; $^{238}U/^{235}U = 137.818 \pm 0.045$ Hiess et al. (2012); $^{234}U/U = (5.5 \pm 0.1) \times 10^{-5}$ Villa et al. (2016).

Table 2. Comparison of half-life values ($t_{1/2}$, in years) of long-lived radionuclides.

	NNDC	**Geochronology**			**NNDC vs. Geo**
Nuclide	$t_{1/2}(\pm)$	$t_{1/2}(\pm)$	%±	Ref.	% rel. difference
^{40}K	$1.248(3) \times 10^{9}$	$1.262(2) \times 10^{9}$	0.2	Naumenko-Dèzes et al. (2018)	−1.1
^{87}Rb	$4.81(9) \times 10^{10}$	$4.961(16) \times 10^{10}$	0.3	Villa et al. (2015)	−3.0
^{138}La	$1.03(1) \times 10^{11}$	$1.03(2) \times 10^{11}$	1.9	Sato & Hirose (1981); Tanimizu (2000)	0
^{147}Sm	$1.07(1) \times 10^{11}$	$1.06(1) \times 10^{11}$	0.9	Begemann et al. (2001)	0
^{176}Lu	$3.76(7) \times 10^{10}$	$3.713(16) \times 10^{10}$	4.3	Söderlund et al. (2004)	1.3
^{187}Re	$4.33(7) \times 10^{10}$	$4.16(4) \times 10^{10}$	1.0	Begemann et al. (2001)	4.1
^{190}Pt	$6.5(3) \times 10^{11}$	$4.899(44) \times 10^{11}$	0.9	Cook et al. (2004)	33
^{232}Th	$1.40(1) \times 10^{10}$	$1.41(1) \times 10^{10}$	1.0	Farley (1960)	−0.7
^{235}U	$7.038(5) \times 10^{8}$	$7.0348(20) \times 10^{8}$	0.03	Hiess et al. (2012)	0.05
^{238}U	$4.4683(24) \times 10^{9}$	$4.4683(96) \times 10^{9}$	0.2	Villa et al. (2016)	0

(±) values with $t_{1/2}$ represent the absolute uncertainty in the last reported significant figure, %± is the relative uncertainty. The relative difference between NNDC (National Nuclear Data Center: `www.nndc.bnl.gov`) and geochronology values are listed in the last column.

Table 3. Long-lived radioactive decay systems in the Earth.

	^{238}U	^{235}U	^{232}Th	^{40}K	^{87}Rb	^{147}Sm
Decay mode	α, β^- chain	α, β^- chain	α, β^- chain	β^- or ε	β^-	α
Natural mole frac.[#]	0.992742	0.0072033	1.0000	1.167×10^{-4}	0.2783	0.14993
Nuclide mass ($\mathrm{g\,mol^{-1}}$)	238.0508	235.0439	232.0381	39.9640	86.9092	146.9149
Atomic mass ($\mathrm{g\,mol^{-1}}$)	238.0289	238.0289	232.038	39.098	85.468	150.362
Decay constant λ ($10^{-18}\,\mathrm{s^{-1}}$)	4.916	31.223	1.558	17.400	0.443	0.207
Decay constant λ ($\mathrm{yr^{-1}}$)	1.5513×10^{-10}	9.8531×10^{-10}	4.916×10^{-11}	5.491×10^{-10}	1.397×10^{-11}	6.539×10^{-12}
Half-life $t_{1/2}$ (10^9 yr)*	4.4683	0.70348	14.1	1.262	49.61	106
1σ uncertainty on $t_{1/2}$ (10^9 yr)	0.0096	0.00020	0.1	0.002	0.16	1
n_α (α particles per decay)	8	7	6	0	0	1
$n_{\bar{\nu}_e}$ (antineutrinos per decay)	6	4	4	0.8944	1	0
n_{ν_e} (neutrinos per decay)	0	0	0	0.1056	0	0
Q (MeV)[†]	51.694	46.397	42.646	1.3313	0.2823	2.3112
Q (pJ)	8.2823	7.4335	6.8326	0.2133	0.0452	0.3703
Q_ν (MeV)	4.050	2.020	2.230	0.655	0.200	0
Q_ν (pJ)[‡]	0.649	0.324	0.357	0.105	0.032	0
Q_h (MeV)	47.6	44.4	40.4	0.676	0.082	2.311
Q_h (pJ)	7.633	7.110	6.475	0.108	0.013	0.370
Element mass frac. (kg/kg)**	2.00×10^{-8}	2.00×10^{-8}	7.54×10^{-8}	2.80×10^{-4}	6.00×10^{-7}	4.06×10^{-7}
Nuclide mass frac. (kg/kg)**	1.99×10^{-8}	0.0144×10^{-8}	7.54×10^{-8}	3.276×10^{-8}	1.67×10^{-7}	6.09×10^{-8}
$l'_{\bar{\nu}_e}$ (kg-element^{-1} s^{-1})	7.636×10^7		1.617×10^7	2.797×10^4	8.682×10^5	0
$L_{\bar{\nu}_e}$ ($\mathrm{s^{-1}}$)	5.99×10^{24}	1.84×10^{23}	4.93×10^{24}	3.17×10^{25}	2.11×10^{24}	0
% contribution to total $L_{\bar{\nu}_e}$	13%	0.41%	11%	71%	4.7%	0
L_{ν_e} ($\mathrm{s^{-1}}$)	0	0	0	3.74×10^{24}	0	0
h (μW/kg) nuclide	94.936	561.65	26.180	29.029	0.04082	0.3073
h' (μW/kg) element	98.293		26.180	0.003387	0.01139	0.04607
H (W)	7.62×10^{12}	3.27×10^{11}	7.98×10^{12}	3.84×10^{12}	2.77×10^{10}	7.56×10^{10}
% contribution to total H	38%	1.6%	40%	19%	0.1%	0.4%

Q is the energy released per decay, Q_ν is the energy carried away by the electron antineutrino or neutrino per decay, Q_h is the energy remaining to provide radiogenic heating per decay, "Nuclide mass frac." and "Element mass frac." are the abundances in silicate Earth within the reference Earth model (i.e., kg of nuclide or element per kg of rock), $l_{\bar{\nu}_e}$ and $l'_{\bar{\nu}_e}$ are the specific antineutrino luminosities of pure nuclide or element (i.e., number of $\bar{\nu}_e$ per kg of nuclide or element per second), $L_{\bar{\nu}_e}$ and L_{ν_e} are the antineutrino and neutrino luminosities of the Earth, h and h' are specific heat production rates of pure nuclide or element, H is the radiogenic heat production of the Earth. Mass of ^{4}He is 4.002603254 u and conversion of amu to MeV is 931.494. Mass of silicate Earth of 4.042×10^{24} kg is used to calculate $L_{\bar{\nu}_e}$, L_{ν_e}, H. [#]values from Table 1; *values from Table 2 Geochronology section; **values from W. F. McDonough & Sun (1995); Arevalo Jr. et al. (2009) and Th/U ratio from Wipperfurth et al. (2018). [‡]Energy removed from the Earth by the $\bar{\nu}_e$ in the U and Th decay chains was calculated by integrating the anti-neutrino spectrum reported by S. Enomoto: www.awa.tohoku.ac.jp/∼sanshiro/research/geoneutrino/spectrum.

Table 4. Short-lived radioactive decay systems in the Earth.

Decay system	Decay mode	Shape factor $S(p,q)$	Q (MeV)	Q_h (MeV)	$t^{\ddagger}_{1/2}$	$(\tilde{h}/A)$ [nW/kg-elem] at $t_{\rm zero}$ (CAI)	Mole frac. (%) parent nuclide	Reference
^{41}Ca $\rightarrow$ ^{41}K	EC	–	0.4217	0	$9.94(15) \times 10^4$	0	$(^{41}\mathrm{Ca}/^{40}\mathrm{Ca})_i = (4.2\pm1.9)\times10^{-9}$	Liu (2017)
^{99}Tc $\rightarrow$ ^{99}Ru	β^-	$0.54p^2+q^2$ (M15)	0.2975	0.0957	$2.111(12) \times 10^5$	46.71	$(^{99}\mathrm{Tc}/^{100}\mathrm{Ru})_i = <3.9\times10^{-5}$	Wasserburg et al. (1994)
^{81}Kr $\rightarrow$ ^{81}Br	EC	–	0.2809	0.0008	$2.29(11) \times 10^5$	–	*not available*	–
^{126}Sn $\rightarrow$ ^{126}Te	β^-, β^-	1$^!$, NuDat$^!$	4.0502	2.8597	$2.35(7) \times 10^5$	3.773×10^4	$(^{126}\mathrm{Sn}/^{124}\mathrm{Sn})_i = \leq3\times10^{-3}$	Brennecka et al. (2017)
^{36}Cl $\rightarrow$ ^{36}Ar	β^- (98.1%)	M15	0.7095	0.3343	$3.01(2) \times 10^5$	0.9557	$(^{36}\mathrm{Cl}/^{35}\mathrm{Cl})_i = (1.9\pm0.5)\times10^{-8}$	Turner et al. (2013)
^{36}Cl $\rightarrow$ ^{36}S	ε (1.9%)	NuDat$^!$	1.1421$^{\rm EC}$	7×10^{-6}	$3.01(2) \times 10^5$	2.011×10^{-5}	"	"
^{79}Se $\rightarrow$ ^{79}Br	β^-	p^2+q^2 [th.]	0.1506	0.0559	$3.26(28) \times 10^5$	–	*not available*	–
^{26}Al $\rightarrow$ ^{26}Mg	EC (18.3%)	–	4.0044	0.3610	$\lambda_{\rm EC}/\lambda = 0.1827$	2057		
^{26}Al $\rightarrow$ ^{26}Mg	β^+ (81.7%)	$p^4+\frac{10}{3}p^2q^2+q^4$ [th.]	2.9824	2.7593	$\lambda_{\beta^+}/\lambda = 0.8173$	1.572×10^4		
^{26}Al $\rightarrow$ ^{26}Mg	Overall			3.1203	$7.17(24) \times 10^5$	1.777×10^4	$(^{26}\mathrm{Al}/^{27}\mathrm{Al})_i = (5.2\pm0.2)\times10^{-5}$	Kita et al. (2013)
^{10}Be $\rightarrow$ ^{10}B	β^-	$p^4+\frac{10}{3}p^2q^2+q^4$ [th.]	0.5568	0.2527	$1.387(12) \times 10^6$	2.270×10^4	$(^{10}\mathrm{Be}/^{9}\mathrm{Be})_i = (5.3\pm1.0)\times10^{-4}$	Liu et al. (2010)
^{93}Zr $\rightarrow$ ^{93}Nb	β^-	p^2+q^2 [th.]	0.0903	0.0456	$1.61(5) \times 10^6$	–	*not available*	–
^{150}Gd $\rightarrow$ ^{146}Sm	α	–	2.8077	2.8077	$1.79(8) \times 10^6$	–	*not available*	–
^{135}Cs $\rightarrow$ ^{135}Ba	β^-	$0.10p^2+q^2$ (M15)	0.2688	0.0615	$2.3(3) \times 10^6$	119.4	$(^{135}\mathrm{Cs}/^{133}\mathrm{Cs})_i = (2.8\pm2)\times10^{-4}$	Bermingham et al. (2014)
^{60}Fe $\rightarrow$ ^{60}Ni	β^-, β^-	1$^!$, NuDat$^!$	3.0598	2.7077	$2.62(4) \times 10^6$	1.367	$(^{60}\mathrm{Fe}/^{56}\mathrm{Fe})_i = (3.8\pm6.9)\times10^{-8}$	Trappitsch et al. (2018)
^{154}Dy $\rightarrow$ ^{150}Gd	α	–	2.9451	2.9451	$3.0(15) \times 10^6$	–	*not available*	–
^{53}Mn $\rightarrow$ ^{53}Cr	EC	–	0.5968	0	$3.74(4) \times 10^6$	0	$(^{53}\mathrm{Mn}/^{55}\mathrm{Mn})_i = (6.5\pm1.9)\times10^{-6}$	Trinquier et al. (2008)
^{98}Tc $\rightarrow$ ^{98}Ru	β^-	1$^!$	1.794	1.5165	$4.2(3) \times 10^6$	1449	$(^{98}\mathrm{Tc}/^{98}\mathrm{Ru})_i = <1.5\times10^{-3}$	Becker & Walker (2003)
^{97}Tc $\rightarrow$ ^{97}Mo	EC	–	0.3247	0	$4.21(16) \times 10^6$	0	$(^{97}\mathrm{Tc}/^{98}\mathrm{Ru})_i = <2\times10^{-5}$	Dauphas et al. (2003)
^{107}Pd $\rightarrow$ ^{107}Ag	β^-	p^2+q^2 [th.]	0.0341	0.0133	$6.5(3) \times 10^6$	0.2768	$(^{107}\mathrm{Pd}/^{108}\mathrm{Pd})_i = (2.573\pm0.07)\times10^{-5}$	Matthes et al. (2017)
^{182}Hf $\rightarrow$ ^{182}W	β^-, β^-	p^2+q^2 [th.], NuDat$^!$	2.1958	1.8276	$8.90(9) \times 10^6$	87.07	$(^{182}\mathrm{Hf}/^{180}\mathrm{Hf})_i = (1.018\pm0.043)\times10^{-4}$	Kruijer et al. (2014)
^{129}I $\rightarrow$ ^{129}Xe	β^-	$p^2+3.16q^2$ (M15)	0.1889	0.0853	$1.57(4) \times 10^7$	12.71	$(^{129}\mathrm{I}/^{127}\mathrm{I})_i = (1.4\pm0.1)\times10^{-4}$	Gilmour & Crowther (2017)
^{205}Pb $\rightarrow$ ^{205}Tl	EC	–	0.05067	0	$1.73(7) \times 10^7$	0	$(^{205}\mathrm{Pb}/^{204}\mathrm{Pb})_i = (1.0\pm0.4)\times10^{-3}$	Baker et al. (2010)
^{92}Nb $\rightarrow$ ^{92}Zr	EC	–	2.0059	1.4956	$3.47(24) \times 10^7$	16.71	$(^{92}\mathrm{Nb}/^{93}\mathrm{Nb})_i = (1.7\pm0.6)\times10^{-5}$	Iizuka et al. (2016)
^{244}Pu $\rightarrow$ ^{232}Th	3α, $2\beta^-$ †	NuDat$^!$	17.0836	15.6264	$8.11(3) \times 10^7$	1.363×10^4	$(^{244}\mathrm{Pu}/^{238}\mathrm{U})_i = 0.008$	Turner et al. (2007)
^{146}Sm $\rightarrow$ ^{142}Nd	α	–	2.5288	2.5288	$1.03(5) \times 10^8$	77.55	$(^{146}\mathrm{Sm}/^{144}\mathrm{Sm})_i = (8.28\pm44)\times10^{-3}$	Marks et al. (2014); Meissner et al.

Q is the energy of transition (Q value) not accounting for possible branching; Q_h is the energy that remains in the Earth to provide radiogenic heating per decay, accounting for branching. M15 = shape factor from Mougeot (2015). $^!$In some cases, we use shape factors equal to 1 or NuDat-tabulated mean electron energies for forbidden transitions, due to lack of better inputs. $^{\rm EC}$Reports the Q value of EC branch. ‡ Half-lives are from NNDC (www.nndc.bnl.gov). Heating coefficients $(\tilde{h}/A)$ (in nW kg-elem^{-1}), so that radiogenic power per unit mass of rock $\tilde{h}$ can be calculated from $\tilde{h} = (\tilde{h}/A) \times A$, A being the elemental mass fraction (kg-element/kg-rock), are obtained similarly to equation (6). † ^{244}Pu also undergoes spontaneous fission to $^{130-136}$Xe isotopes with a fission branching probability of 0.12%. The individual decay energies for the double β^- steps are as follows: ^{126}Sn $\rightarrow$ ^{126}Te: $Q = 0.3782 + 3.6720 = 4.0502$ MeV; ^{60}Fe $\rightarrow$ ^{60}Ni: $Q = 0.237 + 2.8228 = 3.0598$ MeV; ^{182}Hf $\rightarrow$ ^{182}W: $Q = 0.3813 + 1.8145 = 2.1958$ MeV. The individual decay energies for ^{244}Pu $\rightarrow$ ^{232}Th: $Q = 4.6655 + 0.3991 + 2.1901 + 5.2558 + 4.5731 = 17.0836$ MeV